

Geophysical Research Letters[®]

RESEARCH LETTER

10.1029/2022GL099436

Key Points:

- We perform three-dimensional measurements of the trajectories of air bubbles entrained by breaking waves
- The concentration of bubbles decays exponentially below the wave troughs
- Bubbles are transported downstream significantly faster than the Stokes drift during their first wave period underwater

Supporting Information:

Supporting Information may be found in the online version of this article.

Correspondence to:

L. Deike,
ldeike@princeton.edu

Citation:

Ruth, D. J., Néel, B., Erinin, M. A., Mazzatenta, M., Jaquette, R., Veron, F., & Deike, L. (2022). Three-dimensional measurements of air entrainment and enhanced bubble transport during wave breaking. *Geophysical Research Letters*, 49, e2022GL099436. <https://doi.org/10.1029/2022GL099436>

Received 4 MAY 2022
Accepted 19 JUL 2022

Author Contributions:

Data curation: Daniel J. Ruth, Baptiste Néel, Martin A. Erinin, Megan Mazzatenta, Robert Jaquette
Formal analysis: Daniel J. Ruth
Investigation: Daniel J. Ruth, Luc Deike
Methodology: Daniel J. Ruth, Baptiste Néel, Martin A. Erinin, Megan Mazzatenta, Fabrice Veron, Luc Deike
Writing – original draft: Daniel J. Ruth, Luc Deike
Writing – review & editing: Daniel J. Ruth, Baptiste Néel, Martin A. Erinin, Megan Mazzatenta, Robert Jaquette, Fabrice Veron, Luc Deike

Three-Dimensional Measurements of Air Entrainment and Enhanced Bubble Transport During Wave Breaking

Daniel J. Ruth¹ , Baptiste Néel¹ , Martin A. Erinin¹ , Megan Mazzatenta¹ , Robert Jaquette² , Fabrice Veron² , and Luc Deike^{1,3} 

¹Department of Mechanical and Aerospace Engineering, Princeton University, Princeton, NJ, USA, ²School of Marine Science and Policy, University of Delaware, Lewes, DE, USA, ³High Meadows Environmental Institute, Princeton University, Princeton, NJ, USA

Abstract We experimentally investigate the depth distributions and dynamics of air bubbles entrained by breaking waves in a wind-wave channel over a range of breaking wave conditions using high-resolution imaging and three-dimensional bubble tracking. Below the wave troughs, the bubble concentration decays exponentially with depth. Patches of entrained bubbles are identified for each breaking wave, and statistics describing the horizontal and vertical transport are presented. Aggregating our results, we find a stream-wise transport faster than the associated Stokes drift and modified Stokes drift for buoyant particles, which is an effect not accounted for in current models of bubble transport. This enhancement in transport is attributed to the flow field induced by the breaking waves and is relevant for the transport of bubbles, oil droplets, and microplastics at the ocean surface.

Plain Language Summary Air bubbles are produced when waves break at the ocean surface. The additional air-water surface area they introduce enhances the global transfer of gases such as carbon dioxide and oxygen from the atmosphere to the ocean. Understanding the dynamics of these air bubbles, in particular their residence time under water, is necessary to improve bubble-mediated gas transfer models. Such knowledge is also critical in predicting the dispersion of oil spills and the transport of buoyant particles like microplastics in the turbulent environment created by breaking waves. We use three-dimensional measurements of air bubbles produced by breaking waves in a laboratory experiment to show that bubbles typically move in the direction of the wave faster than they would under linear waves due to the effects of wave breaking, and that the bubbles are typically injected to a depth underwater that is related to the height of the wave that breaks.

1. Introduction

When waves break on the ocean surface, the air that is entrained forms bubbles from which gases diffuse into the water, significantly enhancing the air-sea transfer of gases such as oxygen and carbon dioxide (Deike, 2022; Garbe et al., 2014; Reichl & Deike, 2020). After their entrainment, the bubbles can be advected deeper under the water surface by the velocity field generated by the breaking wave as well as Langmuir turbulence (Liang et al., 2011, 2012; Melville et al., 2002). Sufficiently large bubbles will rise back to the surface due to their buoyancy, with their trajectories modulated by the surrounding wave field and the turbulence induced by the breaking wave. Understanding the depths to which bubbles are entrained and their dynamics immediately after their entrainment, when the effects of breaking waves may dominate, is an important component of understanding their transport in the ocean, with implications on the average bubble residence time considered in gas transfer models (Deike & Melville, 2018; Keeling, 1993; Woolf & Thorpe, 1991).

Further, the underlying physics is applicable to a broad range of wave-induced transport problems, such as the dispersion of plastic pollution and oil released in oil spills (Van Sebille et al., 2020). As a consequence, the transport of buoyant or inertial particles by waves has recently received significant attention, but work has primarily focused on transport under (nearly) linear wave fields (Eames, 2008; van den Bremer & Breivik, 2017; Clark et al., 2020; DiBenedetto et al., 2022; van den Bremer et al., 2019). Realistic ocean surface conditions at moderate to high wind speeds, on the other hand, will involve significant breaking waves and modified particle transport (Deike et al., 2017; Pizzo et al., 2019).

In an idealized linear, deep-water wave flow, the time-averaged (Eulerian) velocity is zero at any location beneath the wave troughs. However, Lagrangian particles following the flow are slowly advected in the direction of the

wave, as each orbital “loop” they undertake ends slightly farther downstream than it began, creating a *Stokes drift* in the Lagrangian sense (van den Bremer & Breivik, 2017) which has been observed during the passage of a wave packet in wave channel experiments (van den Bremer et al., 2019). For a linear, single-component deep-water wave, the Stokes drift velocity in the stream-wise direction is given by

$$u_{x,SD} = (ak)^2 c \exp(2kz), \quad (1)$$

with a the wave amplitude, k the wavenumber, $c = \sqrt{g/k}$ the phase velocity where g is the gravitational acceleration, and z the depth.

The action of wave breaking has been shown to significantly enhance the transport of particles near or at the surface relative to their Stokes drift in the non-breaking case. Deike et al. (2017) performed direct numerical simulations of breaking waves and showed an increased drift of almost an order of magnitude, proposing scalings for the transport of particles at the surface and below during the wave period immediately after breaking. Lenain et al. (2019) and Sinnis et al. (2021) confirmed these results studying breaking focusing waves in the laboratory. Breaking-induced horizontal transport is highly dependent on the particle's initial position relative to the wave focusing location: significant enhanced transport of surface particles is limited to those originating within approximately one wavelength of this point. Thus, we can expect that the point during the breaking event at which a bubble is entrained will have a significant effect on its total horizontal transport. Pizzo et al. (2019) estimated that wave breaking can provide an additional stream-wise mass transport equivalent to 30% of the Stokes drift in open ocean conditions, accounting for the intermittent nature of wave breaking.

The motion of inertial particles (such as air bubbles) under wave fields differs from that of passive fluid tracers, due to their different density, finite size and non-spherical shape. Li et al. (2017) studied the dispersal of oil droplets during wave breaking, which, like air bubbles, are less dense than the water. Eames (2008) showed that, using the equations of motion for point-like particles experiencing viscous drag, the mean transport of inertial particles can be approximated as the sum of their quiescent settling or rise velocity and the Stokes drift of the carrier field, provided that the particle Stokes number and the ratio between the quiescent settling or rise velocity and the phase speed are both small. DiBenedetto et al. (2018), Clark et al. (2020), and De Leo and Stocchino (2022) numerically and experimentally investigated particle dynamics in non-breaking wave fields, finding effects of particle shape and inertia on settling and dispersion. More recently, DiBenedetto et al. (2022) proposed a modified Stokes drift for an advected particle, accounting for its density, finding an increased (respectively decreased) drift velocity for light (respectively heavy) particles such as bubbles.

The entrainment depth of bubbles (or buoyant particles in general) in a wind-driven breaking wave field and the enhanced transport of bubbles due to wave breaking are both important factors in near ocean surface transport, though they have remained poorly characterized. To address this gap in understanding, in this paper we experimentally investigate the transport of air bubbles that are entrained when waves break in a laboratory wind-wave channel. Section 2 presents the experimental methods. Section 3 investigates the statistics of the depths to which bubbles are entrained. Then, in Section 4, we analyze the dynamics of entrained bubbles, finding an increase in stream-wise transport relative to the Stokes drift that is induced by wave breaking.

2. Experimental Methods

Wind-waves were generated and studied in the wind-wave channel at the University of Delaware's Air-Sea Interaction Laboratory with the experimental setup and measurements sketched in Figure 1. Measurement positions are shown to scale, and the experiment includes measurements of wind speed, wave height, and water velocity, as well as multiple cameras to obtain bubble sizes, positions, and dynamics in three dimensions.

2.1. Wind-Wave Generation and Measurements

The wind-wave channel is 42 m long, 1 m wide, 1.2 m tall, and was filled to a depth of $h = 0.71$ m. The facility is described in detail by Buckley et al. (2020). Waves were generated by a mechanical wavemaker moving with a central frequency f_0 accompanied by side-band components with frequencies $f = f_0 \pm \Delta f_{sb}$, with $\Delta f_{sb} = 0.05$ Hz. The sidebands induce a beating pattern in the wave height that repeats over a $1/\Delta f_{sb} = 20$ s forcing cycle, which is much longer than any other timescale relevant to this study. Air was blown over the waves by a mechanical pump

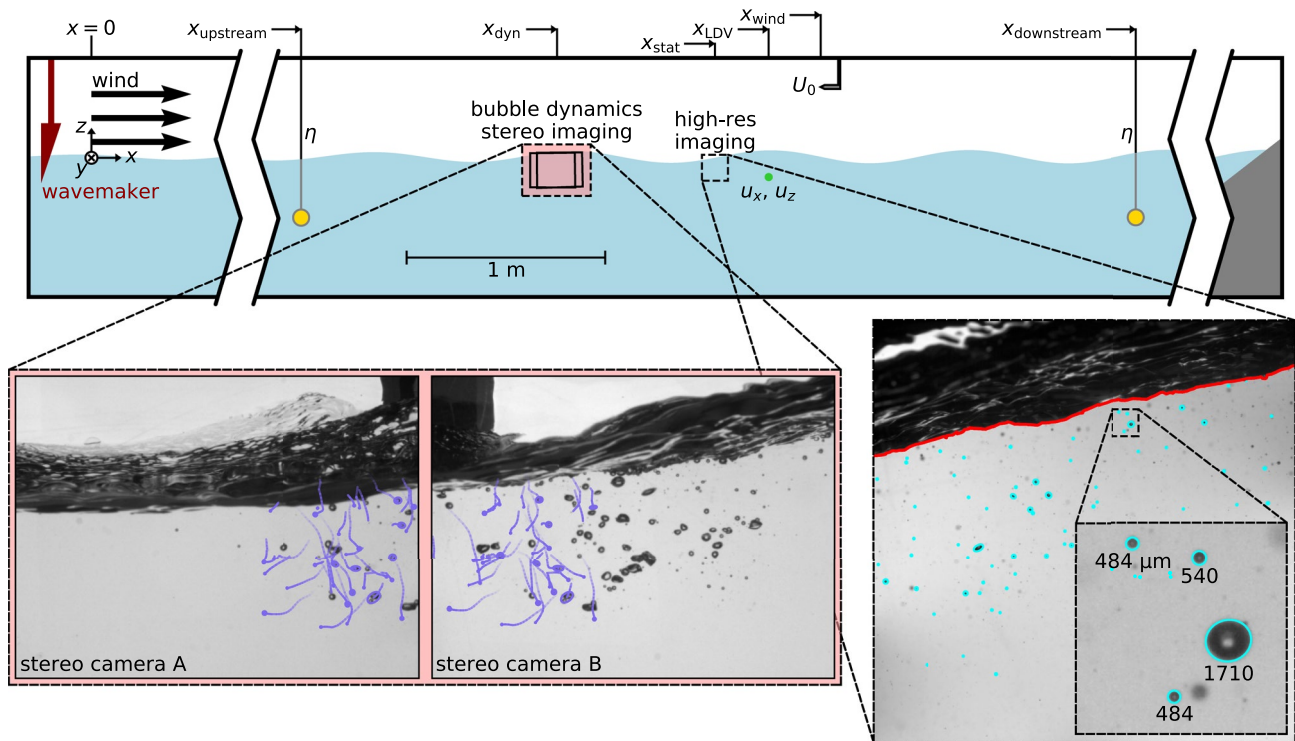


Figure 1. Schematic of the wind-wave facility and bubble measurements. (top) Positions in the $x - z$ plane of the wave gauges measuring $\eta(x_{\text{upstream}}, t)$ and $\eta(x_{\text{downstream}}, t)$, the stereo imaging region at $x = x_{\text{dyn}}$, the high-resolution imaging field of view at $x = x_{\text{stat}}$, the laser Doppler velocimeter measuring $u_x(x_{\text{LDV}}, z_{\text{LDV}}, t)$ and $u_z(x_{\text{LDV}}, z_{\text{LDV}}, t)$, and the pitot tube measuring the wind velocity U_0 at $x = x_{\text{wind}}$. Measurement positions are shown to scale. (bottom left) Simultaneous images from the two synchronized cameras providing a stereo view of the entrained bubbles, with positions and recent trajectories of triangulated bubbles sketched in purple. (bottom right) One high-resolution image, with the detected in-focus bubbles identified in cyan. An inset highlights the detection of small bubbles in one region of the image, with the bubble diameters (in μm) marked.

in a closed-loop circuit, with air returning from the downstream end of the channel to a flow straightener at the upstream end. Each experimental run typically lasted 20 min.

The measurements of air velocity in the stream-wise direction were obtained at a fetch (measured from the outlet of the air flow straightener) of $x_{\text{wind}} = 23.0$ m and vertical position above the mean water level $z_{\text{wind}} = 36$ cm using a Pitot tube recording at 20 Hz, and reported values of U_0 are the time averages of these measurements.

The water surface elevation $\eta(x, t)$ was measured by two modified wave gauges (Akamina AWP-24-3) sketched in Figure 1 recording at 20 Hz. One is positioned 1.3 m upstream of the bubble dynamics measurement (at $x_{\text{upstream}} = 20.37$ m) and another is positioned 2.9 m downstream (at $x_{\text{downstream}} = 24.57$ m). The water surface elevation at the location of the dynamically resolved bubbles is inferred by shifting $\eta(x_{\text{upstream}}, t)$, in order to maximize the correlation between the bubbles' horizontal water velocity v_x and the inferred surface elevation at the bubbles' location $\eta(x, t)$, as is discussed in greater detail in the Supporting Information S1.

The waves studied in this work were generated with either no wavemaker motion (denoted *wind-only* cases, which are only considered in the time-average statistics presented in Section 3) or $f_0 \in (1.0 \text{ Hz}, 1.8 \text{ Hz})$ and air speeds with $U_0 \in (9.0 \text{ m/s}, 11.5 \text{ m/s})$. With lower f_0 , typically just a few of the waves passing during the 20 s forcing period break; at higher forcing frequencies, wave breaking occurs more regularly. Faster wind also increases the wave slopes and the frequency and intensity of breaking. Breaking often begins upstream of the measurement location, but the entire span of the channel that is covered by the measurements involves aspects of breaking (active entrainment, the underwater motion of entrained bubbles, and bubbles floating at the surface, etc.).

From the surface elevation $\eta(x_{\text{upstream}}, t)$ we measure, we compute a characteristic wave amplitude $a_0 = (2\overline{\eta^2})^{1/2}$ and peak frequency f_p , with which we use the dispersion relation $2\pi f_p = \sqrt{gk_p \tanh(k_p h)}$ to calculate the peak

wavenumber k_p and peak phase speed $c_p = 2\pi f_p/k_p$. Surface elevation spectra are shown for each condition in the Supporting Information S1. Over the range of forcing conditions, wavenumbers k_p varied between 3.58 and 9.11 m^{-1} , corresponding to wavelengths $\lambda_p = 2\pi/k_p$ between 0.69 and 1.75 m and phase speeds c_p between 1.04 and 1.64 m/s. Considering these dimensional values, the dimensionless wind speeds ranged from $U_0/c_p = 5.5$ to 10.9, and characteristic wave slopes ranged from $a_0 k_p = 0.17$ to 0.35.

2.2. High-Resolution Imaging of Entrained Bubbles

Statistics on the depths of entrained bubbles were obtained from a high-resolution camera (Basler acA2040-90um) outfitted with a 105 mm lens (Nikon) recording at 5 Hz. The camera was positioned 5 cm below the mean water level at a fetch $x_{\text{stat}} = 22.45$ m, and captured 13×13 cm images with a resolution of $64 \mu\text{m}/\text{pixel}$ and depth of field of approximately 20 cm. Images were back-lit with an LED panel (Phlox) placed just beyond the opposing side of the wind-wave channel.

One image obtained by the camera is shown in the bottom right of Figure 1. In each image, the free surface is first detected (shown as the red line), and then in-focus bubbles below the surface are located and sized using the Canny edge detection technique (Canny, 1986), shown in cyan. We consider bubbles with $d \geq 400 \mu\text{m}$. Depth distributions are computed taking into account the size-dependent depth of field of the imaging system. We note that the free surface likely prevents the detection of bubbles that are just below it, as the surface is often three-dimensional, and the bright light source must be visible behind the bubble to enable its detection.

2.3. Stereo Vision Measurements of Bubble Dynamics

Bubbles entrained by breaking waves were imaged at 200 Hz with two cameras placed 15 cm below the mean water level (Basler acA1440-220um), centered at a fetch $x_{\text{dyn}} = 21.66$ m. The cameras were separated by 24 cm in the stream-wise direction, and were angled slightly inwards such that their fields of view overlap near the middle of the wave channel. The fields of view, sketched in the $x - y$ plane in Figure 4e, first meet near the close ($-y$) face of the wave channel, and share approximately 28 cm in the stream-wise ($+x$) direction 70 cm toward the back face of the tank, beyond which bubbles are too far from the cameras to image accurately. Thus, the imaged domain spans about 22 cm in the middle of the tank. The useable vertical span resolved in the middle of the tank extends from $z = -10$ cm to $z = 2$ cm. Three-dimensional bubble positions are determined by mapping each cameras' pixels to incoming light rays in physical space following Machicoane et al. (2019), and finding the locations at which rays intersecting bubble images nearly coincide, as discussed in Ruth et al. (2021). Individual bubble positions are then linked temporally into bubble trajectories using the Python package Trackpy (Allen et al., 2021), which implements the algorithm from Crocker and Grier (1996). Bubble velocities are obtained by differentiating their three-dimensional positions in time. The pixel size varies spatially with the bubbles' distance from the camera (from about $90 \mu\text{m}/\text{px}$ near the cameras to $190 \mu\text{m}/\text{px}$ far from it). The typical sizes of the detected bubbles range from $400 \mu\text{m}$ to 5 mm. Each recording lasts 3.5 s, and the recording times are staggered to reduce aliasing with the forcing cycle of the wavemaker. Bubble dissolution is negligible over the relatively short duration of the tracking, so individual bubbles do not change size in any significant way during the tracking. One image pair and the positions and recent trajectories of entrained bubbles are shown in the bottom left of Figure 1.

3. Entrained Bubble Depths

First, we consider the depths to which bubbles are entrained at different conditions. Figure 2 shows information on the entrained bubbles for two wavefields: one is characterized by long waves, with $f_0 = 1.2$ Hz and $a_0 k_p = 0.24$ (on the left), and the other is characterized by shorter, steeper waves, with $f_0 = 1.6$ Hz and $a_0 k_p = 0.32$ (on the right). The results presented are data which is ensemble-averaged over approximately 60 realizations of each $1/\Delta f_{\text{sb}} = 20$ s cycle of the wavemaker's motion, over which the instantaneous wave amplitude $a(t)$ modulates.

The top panels give the ensemble-average number of detected bubbles $n(t)$, and the dashed green lines give the ensemble-average wave slope ak_p . In the long-wave case, there are two peaks in $n(t)$, suggesting that there are two instances of entrainment during each forcing cycle. The shaded area around the curve denotes the mean \pm half of a standard deviation of the number of imaged bubbles, suggesting that the two entrainment events are highly

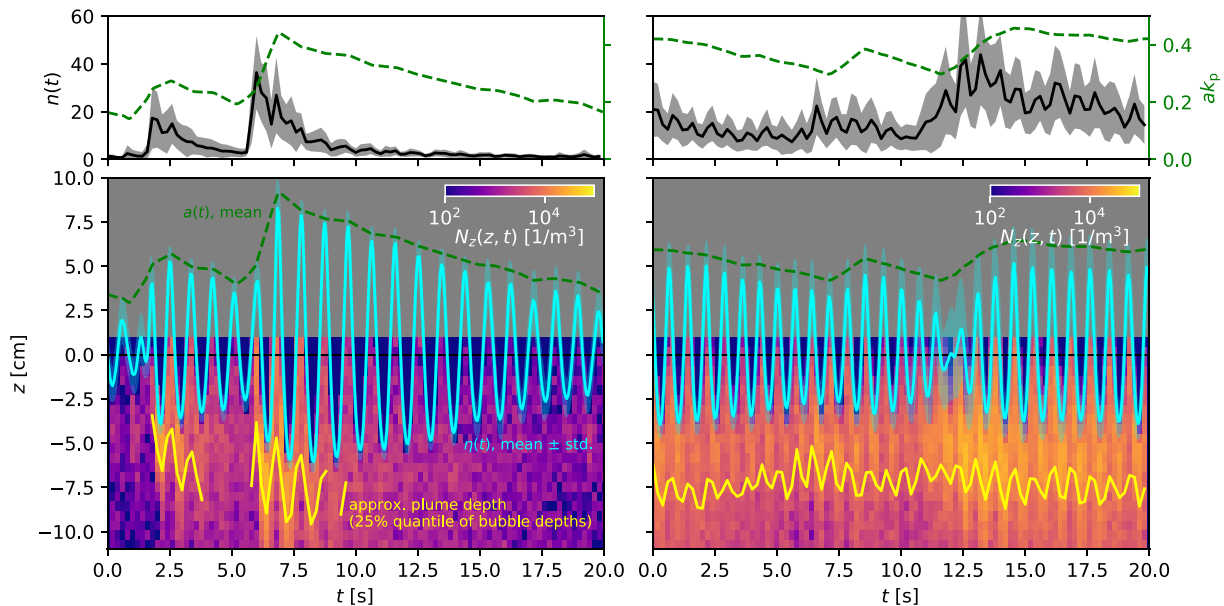


Figure 2. Transient bubble statistics over the $1/\Delta f_{sb} = 20$ s forcing cycle for two cases. The left shows a case with $f_0 = 1.2$ Hz, $U_0 = 11.1$ m/s, $a_0 k_p = 0.23$, and $U_0/c_p = 7.8$ (referred to as the *long-wave* case); the right shows a case with $f_0 = 1.6$ Hz, $U_0 = 11.5$ m/s, $a_0 k_p = 0.32$, and $U_0/c_p = 9.8$ (referred to as the *short-wave* case). Solid lines on the top show the ensemble-average number of bubbles imaged as a function of time, with the shaded area representing \pm one half of a standard deviation around the mean. Plots on the bottom show the transient bubble depth distribution $N_z(z, t)$, with the cyan curve and shaded region giving the ensemble-average surface elevation $\eta \pm$ one standard deviation around the mean. The yellow curve gives the approximate bubble plume depth (taken to be the 25% quantile of bubble depths) over times at which at least 5 bubbles are observed, on average. The dashed green lines give, on the top and bottom, the ensemble-averaged wave slope ak_p and the wave amplitude a , respectively, both based on the amplitude of the instantaneous surface elevation.

repeatable between different iterations of the $1/\Delta f_{sb} = 20$ s wavemaker forcing cycle. In the short-wave case, on the right, the number of bubbles varies less over the forcing cycle, suggesting that the steeper waves are breaking and entraining air more often in this case.

Transient bubble depth distributions $N_z(z, t)$, which give the number of imaged bubbles at a depth z and time t per unit volume (averaged over the horizontal extent of the image), are shown in the bottom panels of Figure 2. Again, there are two peaks in the bubble concentration in the long-wave case, while the bubble depth distribution in the short-wave case is less variable. The field of view extends between approximately $z = -11.1$ cm and $z = 1.7$ cm, so we do not capture most of the bubbles that are in the crests of the waves. The approximate depth of the bubble plume is given by the yellow lines, taken somewhat arbitrarily to be the 25% quantile of bubble depths. Bubbles' concentrations are the highest in the few centimeters below the water surface immediately after entrainment events, with the ensemble-average surface elevation shown in cyan. Here, $\eta(x_{stat}, t)$ is calculated by aligning the upstream surface elevation $\eta(x_{upstream}, t)$ in time with maximum vertical positions of the entrained bubbles.

Figures 3a–3c shows the bubble depth distributions averaged in time over the entire experimental run, $\langle N_z(z) \rangle$, at nine different conditions varying in U_0 (denoted by the color) and the wavemaker forcing. Cases forced only by the wind are shown in (a), while cases with $f_0 = 1.2$ Hz and $f_0 = 1.8$ Hz are shown in (b) and (c), respectively. Increasing the wind speed steepens the waves and increases the number of entrained bubbles for all wave forcing central frequencies. The typical wave amplitude a_0 is denoted for each case by the horizontal dashed line, and the depth at which the concentration of the bubbles is the greatest, shown by the circles, is typically about 1 cm below this peak. As shown in the Supporting Information S1, this peak in $N_z(z)$ corresponds with the minimum position of the water surface over the experimental run. Above this depth, there are fewer opportunities for bubbles to be present (as water is present there only a portion of the time), which contributes to the decrease in $\langle N_z(z) \rangle$ close to the mean water level.

The bubble concentration profiles reported in Figures 3a–3c have markedly different shapes. However, panel (d) shows that each condition shares a common bubble concentration profile, once non-dimensionalized by the typical wave amplitude a_0 and the peak bubble concentration $\langle N_z(z) \rangle_{max}$. The depths within $-2 < z/a_0 < -1$ have

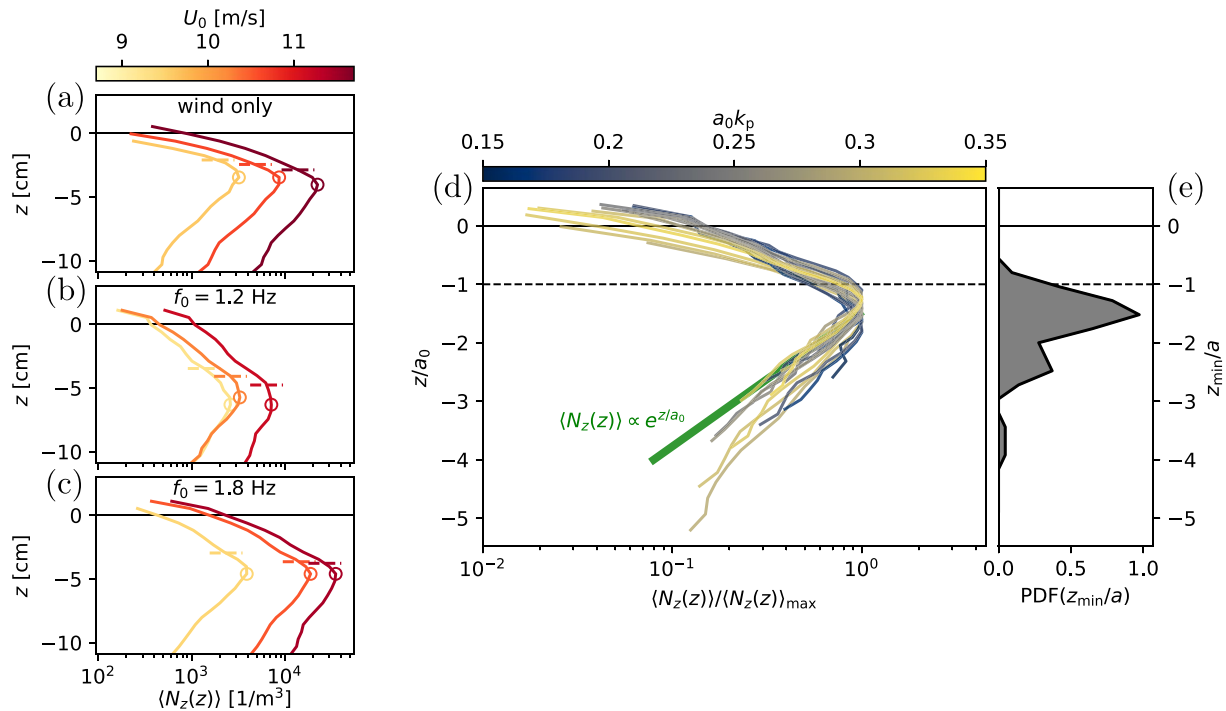


Figure 3. Depths of the entrained bubbles. (a–c) Time-averaged distributions of bubble depths for cases without wavemaker forcing (a) and with central wavemaker forcing frequencies of 1.2 Hz (b) and 1.8 Hz (c). Each line corresponds with a different wind speed U_0 . Dashed lines denote the depth of the typical wave trough $z = -a_0$, and circles denote the mode, where the concentration of bubbles is the highest. (d) Time-averaged bubble depth distributions, with depth normalized by the typical wave amplitude a_0 and the distributions normalized by their peak value. Distributions peak between $z = -a_0$ and $z = -2a_0$, below which they follow an exponential decay with a length scale set by a_0 . The line color denotes the typical wave slope $a_0 k_p$. (e) Distributions of the minimum depth to which bubbles are entrained over their initial period underwater z_{\min} , normalized by the amplitude of the breaking wave a , as determined from the dynamical data presented in Section 4.

the highest concentration of bubbles. At lower depths (where water is always present), the concentration decays exponentially with a length scale set by a_0 , yielding

$$\frac{\langle N_z(z) \rangle}{\langle N_z(z) \rangle_{\max}} = c_z e^{z/a_0} \quad (2)$$

with $c_z = 4.3$ a fitted non-dimensional coefficient, as is indicated by the green line. This exponential decay mirrors results from Hwang et al. (1990), who presented bubble size distributions obtained with an optical sensor and showed they followed an exponential decay in depth set by the height of the breaking wave.

Further, we consider the bubbles which are tracked dynamically immediately after entrainment, which are presented in greater detail in Section 4. The distribution of the minimum depths to which they are advected during their initial period underwater, normalized by the amplitude of the breaking wave a , is shown in Figure 3e. These dynamically tracked bubbles, which are typically larger than those imaged with the high-resolution setup providing the other data in Figure 3, are advected to between $z = -a_0$ and $z = -2a_0$.

Thus, we provide a simple description of bubble concentration profiles under an actively breaking wave field for a wide range of wind and wave conditions, demonstrating that the significant wave height is the controlling factor of the depth concentration profiles. The scaling with the wave amplitude a_0 could enable extrapolation of these results to conditions at sea if provided with knowledge of the temporal evolution of the wave amplitude.

4. Bubble Dynamics Immediately After Entrainment and Enhanced Lagrangian Drift

In this section, we analyze the dynamics of air bubbles during the times immediately after their entrainment by a breaking wave, by manually identifying recordings in which entrainment was captured. First, Section 4.1 details one case of bubble entrainment and illustrates the data processing employed to obtain the wave-averaged

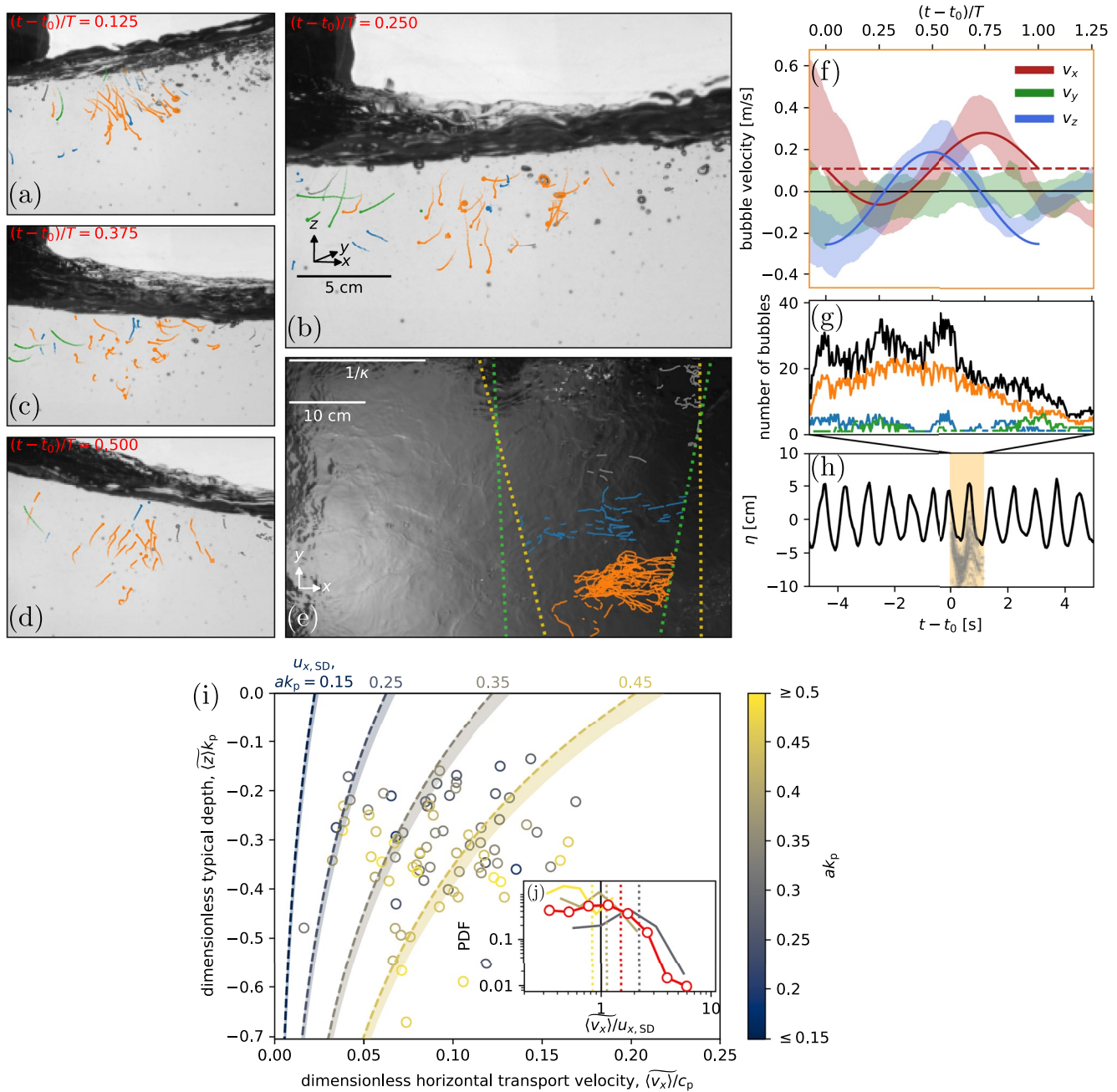


Figure 4. Enhanced bubble transport by wave breaking. (a–d) Side view snapshots from one of the two cameras aligned roughly in the x – z plane, with bubble positions and recent trajectories sketched. (e) Snapshot of the surface, with the bubbles' trajectories sketched. The dotted lines denote the field of view of the two side cameras; the 3-D trajectories are resolved where these fields overlap. The field of view does not cover the entire channel width. (f) The instantaneous mean of each component of the velocities of all bubbles in the orange entrainment patch, \pm one standard deviation. Solid blue and red lines give the fits to the bubble vertical and stream-wise velocities over the first wave period, and the dashed red line gives the mean stream-wise velocity $\langle \overline{v_x} \rangle$. (g) The number of bubbles imaged in total (black) and in each patch (colors). (h) The instantaneous elevation η over a 10 s window at the bubble measurement location. Gray dots show the detected bubble depths as a function of time; that they lie under the surface elevation signal validates the method used to find η . (i) Circles give the mean stream-wise velocity of entrained bubbles, phase-averaged over the first period of their time underwater and normalized by the phase velocity, as a function of their typical depth normalized by the wavenumber. Color maps to the slope of the breaking wave ak_p . Dashed lines give the Stokes drifts associated with various wave slopes, showing that the transport of entrained bubbles is typically magnified relative to the associated Stokes drift. The band extending from each line gives the range of enhanced Lagrangian drifts for bubbles for a wave field with $f_0 = 1.8$ Hz. (j) The distribution of the phase-averaged stream-wise velocity normalized by the modified Stokes drift (based on the local value of a), with the dotted lines denoting the mean. Separate distributions for cases grouped by ak_p are shown in blue, gray, and yellow (corresponding to $ak_p \in (0.15, 0.35], (0.35, 0.45]$, and $(0.45, 0.6)$, respectively); the distribution for the entire data set is shown in red.

velocity (the drift) and the entrainment depth. Then, Section 4.2 compiles these quantities from many individual entrainment events in order to build a statistical picture of the initial horizontal and vertical transport of entrained bubbles.

4.1. Analysis Applied to Bubble Entrainment Observations

Entrainment by one breaking wave is illustrated in Figures 4a–4h, with a complementary movie (and movies of similar events) given as Supporting Information S1. Panels (a–d) show four snapshots from one of the two cameras used for the stereo triangulation, and detected bubbles and their recent trajectories (fading away over 0.1 s) are sketched. Panel (e) shows one snapshot of the water surface, with the bubbles' (x, y) positions and trajectories sketched. The dotted lines bound the fields of view for the two cameras used in the triangulation; that of the view shown in (a–d) is given by the orange lines. The bubbles can only be triangulated in the region in which the views overlap.

The detected bubbles are clustered into *entrainment patches* using the DBSCAN algorithm (Ester et al., 1996) (as detailed in the Supporting Information S1), which takes a collection of points in n -dimensional space and identifies clusters of nearby points. Our implementation considers the bubbles' (x, y, z) positions, but weights the y coordinates such that clusters are more likely to be separated in the span-wise direction. The blue, orange, and green markings in (a–e) denote the positions and recent trajectories of bubbles in the four patches, which differ primarily in their span-wise position. Gray markings denote bubbles not assigned to patches, or patches which do not pass data quality metrics.

Focusing now on the entrainment patch colored orange, bubbles are first detected in the crest of the wave, where their motion is largely in the $+x$ direction with the breaking crest. At $t/T = 0.125$, shown in panel (a), their motion is slightly forwards but primarily downwards. At $t/T = 0.25$, shown in panel (b), the bubbles are advected downwards, and the circuitous path of their trajectories suggests that the flow they are subjected to is turbulent. By $t/T = 0.375$, shown in panel (c), the bubbles begin to rise back toward the surface. They continue their rise under buoyancy and the wave field at $t/T = 0.5$, in panel (d), again traveling in the $+x$ direction.

Figure 4f gives the instantaneous velocity components of the bubbles in the orange entrainment patch, with each band denoting the instantaneous ensemble average $\langle v_i \rangle \pm$ one standard deviation of that component of all the bubbles' detected velocities at that time. The stream-wise component $\langle v_x \rangle(t)$ can be represented by a sinusoidal oscillation around a mean with

$$\langle v_x \rangle_{\text{fit}} = \langle \widetilde{v_x} \rangle - \mathcal{V}_x \sin(2\pi(t - t_0)/T). \quad (3)$$

Here, the fit values $\langle \widetilde{v_x} \rangle$ and \mathcal{V}_x describe, respectively, the mean stream-wise velocity of the bubbles phase-averaged over this initial wave period T underwater, and the amplitude of the horizontal velocity oscillations. The temporal shift t_0 is chosen given a fit of the form $\langle v_z \rangle_{\text{fit}} = \langle \widetilde{v_z} \rangle - \mathcal{V}_z \cos(2\pi(t - t_0)/T)$ applied to the ensemble-averaged motion in the vertical direction, effectively defining t_0 as the time of the maximum downwards bubble velocity. The fits to the horizontal and vertical bubble velocities are shown as the solid red and blue lines, respectively, in Figure 4f, where the dashed red line gives the mean stream-wise bubble velocity $\langle \widetilde{v_x} \rangle$. We similarly fit to the ensemble-median z position $\langle z \rangle$, obtaining $\langle z \rangle_{\text{fit}} = \langle \widetilde{z} \rangle - \mathcal{Z} \sin(2\pi(t - t_0)/T)$, which yields the characteristic depth $\langle \widetilde{z} \rangle$ for the event. Having performed the fits, we discard any entrainment clusters for which the r^2 value describing the relationship between $\langle v_x \rangle$ and $\langle v_x \rangle_{\text{fit}}$ is less than 0.75.

Figure 4g shows the number of bubbles detected over time in each entrainment patch (in the colored lines) and in total (in black); panels (a–d) suggest that most bubbles are not detected, due to the inherent difficulties in imaging a high-void-fraction multiphase flow with just two cameras, but we take the bubbles we do detect to be representative of the entire entrained population.

Finally, Figure 4h shows the surface elevation at the approximate bubble location $\eta(x_{\text{dyn}}, t)$, as determined with the method described in the Supporting Information S1. We estimate the breaking wave amplitude a for the entrainment patch by taking the maximum value of the function enveloping $|\eta(t)|$ within $t \in (t_0 - T, t_0 + T)$. The time frame over which the bubbles in the illustrated entrainment event are detected (lasting approximately 1.5 T)

is highlighted in orange. The depths of every detected bubble are plotted as a function of time in gray, confirming that our surface elevation translation yields a local water level that is consistent with the measured bubble positions.

4.2. Enhanced Horizontal Drift After Entrainment

Figure 4i aggregates data from 87 entrainment patches to present an analysis of the bubbles' stream-wise transport during their first wave period underwater. Each point, colored by the breaking wave slope ak_p , shows the phase-averaged Lagrangian velocity, $\langle \widetilde{v_x} \rangle$, normalized by the wave phase speed c_p , as a function of the dimensionless typical depth to which the bubble cluster is injected, $\langle z \rangle k_p$. We observe net drifts with $\langle \widetilde{v_x} \rangle / c_p$ ranging from approximately 0.05 to 0.15. Dashed lines give the corresponding dimensionless Stokes drifts $u_{x,SD} / c_p$ from Equation 1 (using $k = k_p$) as functions of depth for various wave slopes, evidencing that entrained bubbles are typically transported downstream with velocities significantly higher than the Stokes drift during the period following entrainment.

This enhanced transport is made evident in Figure 4j, in which the red curve gives the distribution of $\langle \widetilde{v_x} \rangle / u_{x,SD}$ for all the entrainment patches, and the dotted red line gives the mean of this distribution, which is 1.5. Many entrainment patches have a horizontal transport velocity comparable to the Stokes drift, while some exhibit a transport that is multiple times greater. The blue, gray, and yellow curves give the distributions for cases with $ak_p \in (0.15, 0.35]$, $(0.35, 0.45]$, and $(0.45, 0.6)$, respectively. Deike et al. (2017) found that, while the dimensionless Stokes drift scales with the wave slope as $u_{x,SD} / c_p \propto (ak_p)^2$, the dimensionless breaking-induced drift scales as $\propto ak_p$, and our experimental data suggests a similar trend (in that $\langle \widetilde{v_x} \rangle / u_{x,SD}$ tends to decrease as the wave slope ak_p increases). There is significant scatter in the data, likely due in part to the bubbles' relative positions within the breaking wave, which has been shown to have a strong effect on enhanced fluid transport (Deike et al., 2017).

We comment here on the importance of considering the instantaneous slope of the wave that breaks ak_p rather than a_0k_p , which is a single descriptor of the typical wave slope for an inhomogeneous field. Since steeper waves are the ones which tend to break, the values of ak_p ascribed to the entrainment patches tend to exceed the wave field's typical slope a_0k_p by 42% in our data set, and the Stokes drifts computed with a_0k_p are typically just 59% of those associated with the breaking wave slope ak_p . Had we considered just the typical wave slope a_0k_p in our analysis, we would have concluded that the typical breaking-induced drift is much greater relative to the Stokes drift than the increase demonstrated in Figures 4i and 4j.

DiBenedetto et al. (2022) derived a modified Stokes drift for particles with different density than the surrounding water in a non-breaking wave field. Light particles such as bubbles experience a Lagrangian drift $v_{x,SD}$ that is increased relative to the Stokes drift $u_{x,SD}$, due to their decreased density and buoyant rise. This effect is shown by the colored bands extending to the right of the Stokes drift curves for each wave slope, denoting the range of Lagrangian drift velocities taken by bubbles with $d = 0.5\text{--}5$ mm in a wave field with a peak frequency $f_p = 1.8$ Hz, which amounts to at most a 10% increase relative to the tracer particle Stokes drift.

The large values of $\langle \widetilde{v_x} \rangle$ relative to the Stokes drift shown in Figure 4j are not explained by these particle density corrections. Rather, the enhanced transport of bubbles we observe during their entrainment mirrors the enhanced transports of fluid parcels simulated (Deike et al., 2017) and nearly neutral density particles measured experimentally (Lenain et al., 2019; Sinnis et al., 2021) during wave breaking. Upscaling the present results from the laboratory to the ocean scales could be done by leveraging the wave breaking distribution framework (Phillips, 1985; Sutherland & Melville, 2013) applied to surface transport of particles by breaking, as proposed by Pizzo et al. (2019).

5. Concluding Remarks

Through three-dimensional measurements of the dynamics of bubbles entrained by wind-driven breaking waves, we characterize the depths to which the bubbles are entrained and the enhanced stream-wise drifts they experience. We show that bubbles are the most highly concentrated near the troughs of waves which break, with faster wind leading to a deeper injection as the wave amplitude grows. We characterize the depth concentration profiles

of the entrained bubbles and show an exponential decay with depth, with an e-folding scale controlled by the wave height.

Finally, we characterize the Lagrangian drift of the bubbles during the entrainment stage and observe an enhancement of the initial stream-wise transport relative to the classic Stokes drift associated with a linear, non-breaking wave field, mirroring recent findings on the transport of particles by wave breaking. Accounting for this breaking-induced transport in regions where breaking is known to be occurring should be seen as a necessary component in modeling the surface transport of bubbles and other buoyant particles, such as microplastics and droplets from oil spills.

Data Availability Statement

Data and code to reproduce plots in this paper are publicly available at <https://doi.org/10.34770/0q6b-cj27>.

Acknowledgments

The support of the Division of Ocean Sciences of the National Science Foundation under grant OCE2122042 to LD and OCE1829660 to FV are gratefully acknowledged. This work was also supported by the Collaborative Institute for Modeling the Earth System between NOAA GFDL and Princeton University. This material is based upon work supported by the National Science Foundation Graduate Research Fellowship awarded to MM. DJR, BN, MAE, MM, FV, and LD designed the experiments; DJR, MAE, BN, MM, and RDJ collected wave and wind data. DJR performed stereoscopic tracking measurements, DJR and LD analyzed data and wrote the paper; all authors edited the paper.

References

- Allen, D. B., Caswell, T. A., Keim, N. C., van der Wel, C., & Verweij, R. (2021). Trackpy. <https://doi.org/10.5281/zenodo.4682814>
- Buckley, M. P., Veron, F., & Yousefi, K. (2020). Surface viscous stress over wind-driven waves with intermittent airflow separation. *Journal of Fluid Mechanics*, 905, A31. <https://doi.org/10.1017/jfm.2020.760>
- Canny, J. (1986). A computational approach to edge detection. *IEEE Transactions on Pattern Analysis and Machine Intelligence, PAMI-*, 8(6), 679–698. <https://doi.org/10.1109/TPAMI.1986.4767851>
- Clark, L. K., Dibenedetto, M. H., Ouellette, N. T., & Koseff, J. R. (2020). Settling of inertial nonspherical particles in wavy flow. *Physical Review Fluids*, 5(12), 124301. <https://doi.org/10.1103/PhysRevFluids.5.124301>
- Crocker, J., & Grier, D. (1996). Methods of digital video microscopy for colloidal studies. *Journal of Colloid and Interface Science*, 179(1), 298–310. <https://doi.org/10.1006/jcis.1996.0217>
- Deike, L. (2022). Mass transfer at the ocean–atmosphere interface: The role of wave breaking, droplets, and bubbles. *Annual Review of Fluid Mechanics*, 54(1), 191–224. <https://doi.org/10.1146/annurev-fluid-030121-014132>
- Deike, L., & Melville, W. K. (2018). Gas transfer by breaking waves. *Geophysical Research Letters*, 45(19), 482–510. <https://doi.org/10.1029/2018GL078758>
- Deike, L., Pizzo, N., & Melville, W. K. (2017). Lagrangian transport by breaking surface waves. *Journal of Fluid Mechanics*, 829, 364–391. <https://doi.org/10.1017/jfm.2017.548>
- De Leo, A., & Stocchino, A. (2022). Dispersion of heavy particles under sea waves. *Physics of Fluids*, 34(1), 013305. <https://doi.org/10.1063/5.0074760>
- DiBenedetto, M. H., Clark, L. K., & Pujara, N. (2022). Enhanced settling and dispersion of inertial particles in surface waves. *Journal of Fluid Mechanics*, 936, A38. <https://doi.org/10.1017/jfm.2022.95>
- DiBenedetto, M. H., Ouellette, N. T., & Koseff, J. R. (2018). Transport of anisotropic particles under waves. *Journal of Fluid Mechanics*, 837, 320–340. <https://doi.org/10.1017/jfm.2017.853>
- Eames, I. (2008). Settling of particles beneath water waves. *Journal of Physical Oceanography*, 38(12), 2846–2853. <https://doi.org/10.1175/2008JPO3793.1>
- Ester, M., Kriegel, H.-P., Sander, J., & Xu, X. (1996). A density-based algorithm for discovering clusters in large spatial databases with noise. In *Kdd-96*. Elsevier.
- Garbe, C. S., Rutgersson, A., Boutin, J., Leeuw, G. D., Delille, B., Fairall, C. W., et al. (2014). Ocean-atmosphere interactions of gases and particles. Retrieved from <http://link.springer.com/10.1007/978-3-642-25643-1>
- Hwang, P. A., Hsu, Y.-H. L., & Wu, J. (1990). Air bubbles produced by breaking wind waves. *A Laboratory Study*, 20(1), 19–28. [https://doi.org/10.1175/1520-0485\(1990\)020<0019:abpbw>2.0.co;2](https://doi.org/10.1175/1520-0485(1990)020<0019:abpbw>2.0.co;2)
- Keeling, R. F. (1993). On the role of large bubbles in air-sea gas exchange and supersaturation in the ocean. *Journal of Marine Research*, 51(2), 237–271. <https://doi.org/10.1357/0022240933223800>
- Lenain, L., Pizzo, N., & Melville, W. K. (2019). Laboratory studies of Lagrangian transport by breaking surface waves. *Journal of Fluid Mechanics*, 876, 1–12. <https://doi.org/10.1017/jfm.2019.544>
- Li, C., Miller, J., Wang, J., Koley, S. S., & Katz, J. (2017). Size distribution and dispersion of droplets generated by impingement of breaking waves on oil slicks. *Journal of Geophysical Research: Oceans*, 122(10), 7938–7957. <https://doi.org/10.1002/2017jc013193>
- Liang, J. H., McWilliams, J. C., Sullivan, P. P., & Baschek, B. (2011). Modeling bubbles and dissolved gases in the ocean. *Journal of Geophysical Research*, 116(3), 1–17. <https://doi.org/10.1029/2010JC006579>
- Liang, J. H., McWilliams, J. C., Sullivan, P. P., & Baschek, B. (2012). Large eddy simulation of the bubbly ocean: New insights on subsurface bubble distribution and bubble-mediated gas transfer. *Journal of Geophysical Research*, 117(4), 1–14. <https://doi.org/10.1029/2011JC007766>
- Machicoane, N., Aliseda, A., Volk, R., & Bourgoin, M. (2019). A simplified and versatile calibration method for multi-camera optical systems in 3D particle imaging. *Review of Scientific Instruments*, 90(3), 035112. <https://doi.org/10.1063/1.5080743>
- Melville, W. K., Veron, F., & White, C. J. (2002). The velocity field under breaking waves: Coherent structures and turbulence. *Journal of Fluid Mechanics*, 454, 203–233. <https://doi.org/10.1017/S0022112001007078>
- Phillips, O. M. (1985). Spectral and statistical properties of the equilibrium range in wind-generated gravity waves. *Journal of Fluid Mechanics*, 156(1), 505. <https://doi.org/10.1017/S0022112085002221>
- Pizzo, N., Melville, W. K., & Deike, L. (2019). Lagrangian transport by nonbreaking and breaking deep-water waves at the ocean surface. *Journal of Physical Oceanography*, 49(4), 983–992. <https://doi.org/10.1175/JPO-D-18-0227.1>
- Reichl, B., & Deike, L. (2020). Contribution of sea-state dependent bubbles to air-sea carbon dioxide fluxes. *Geophysical Research Letters*, 47(9), e2020GL087267. <https://doi.org/10.1029/2020gl087267>
- Ruth, D. J., Vernet, M., Perrard, S., & Deike, L. (2021). The effect of nonlinear drag on the rise velocity of bubbles in turbulence. *Journal of Fluid Mechanics*, 924, A2. <https://doi.org/10.1017/jfm.2021.556>

- Sinnis, J. T., Grare, L., Lenain, L., & Pizzo, N. (2021). Laboratory studies of the role of bandwidth in surface transport and energy dissipation of deep-water breaking waves. *Journal of Fluid Mechanics*, 927, 1–23. <https://doi.org/10.1017/jfm.2021.734>
- Sutherland, P., & Melville, W. K. (2013). Field measurements and scaling of ocean surface wave-breaking statistics. *Geophysical Research Letters*, 40(12), 3074–3079. <https://doi.org/10.1002/grl.50584>
- van den Bremer, T. S., & Breivik, O. (2017). Stokes drift. In *Philosophical transactions. Series A, mathematical, physical, and engineering sciences*.
- van den Bremer, T. S., Whittaker, C., Calvert, R., Raby, A., & Taylor, P. H. (2019). Experimental study of particle trajectories below deep-water surface gravity wave groups. *Journal of Fluid Mechanics*, 879, 168–186. <https://doi.org/10.1017/jfm.2019.584>
- Van Sebille, E., Aliani, S., Law, K. L., Maximenko, N., Alsina, J. M., Bagaev, A., et al. (2020). The physical oceanography of the transport of floating marine debris. *Environmental Research Letters*, 15(2), 023003. <https://doi.org/10.1088/1748-9326/ab6d7d>
- Woolf, D. K., & Thorpe, S. A. (1991). Bubbles and the air-sea exchange of gases in near-saturation conditions. *Journal of Marine Research*, 49(3), 435–466. <https://doi.org/10.1357/002224091784995765>